



Elucidation of Spatiotemporal structures from high-resolution blowing snow observations

Kouichi Nishimura¹, Masaki Nemoto², Yoichi Ito², Satoru Omiya³, Kou Shimoyama⁴, Hirofumi Niiya⁵

¹Nagoya University, Nagoya, 464-8601, Japan

5 ²Snow and Ice Research Center, NIED, Shinjo, 996-0091, Japan

³Civil Engineering Research Institute for Cold Region, PWRI, Sapporo, 996-0091, Japan

⁴Institute of Low Temperature Science, Hokkaido University, Sapporo, 060-0819, Japan

⁵Research Institute for Natural Hazards and Disaster Recovery, Niigata University, Niigata, 950-2181, Japan

Correspondence to: Kouichi Nishimura (knishi99@gmail.com)

10 **Abstract.** Systematic observations were conducted to investigate the spatio-temporal structures of blowing snow. Along a line perpendicular to the dominant wind direction on the leeside of a flat field, fifteen Snow Particle Counters (SPCs) and Ultra Sonic Anemometers (USAs) were placed 1.5 m apart. Data were recorded at high frequencies of 100 kHz for SPCs and 1 kHz for USAs. The horizontal mass flux distributions, representing the spatio-temporal variability of blowing snow, exhibited non-uniformity in both time and space and manifested periodic changes akin to snow waves. Additionally, the presence of 'snow snakes,' meandering near the snow surface, was observed. Quadrant analysis revealed predominant snow fluxes in quadrants Q1 ($u' > 0, w' > 0$) and Q4 ($u' > 0, w' < 0$). However, a more detailed parametric curve analysis indicated the existence of ejection events Q2 ($u' < 0, w' > 0$) before snow waves and in front of snow snakes, shifting to Q1 and Q4 afterward, implying the consideration of both top-down and bottom-up mechanisms for burst sweep events.

1 Introduction

20 The transport of snow by wind, known as blowing or drifting snow, plays a significant role in engineering and climatological contexts. Near roads, blowing snow can cause snow drifts and reduce visibility, leading to traffic accidents. Wind-driven snow redistribution can result in localized snow accumulation and the formation of snow cornices, influencing snow avalanche danger. The impact of katabatic winds on the Antarctic ice sheet affects mass and energy balance, becoming more critical when considering global climate change effects.

25 Numerous investigations have been carried out, both in the field and in wind tunnels, to explore the meteorological conditions that trigger blowing snow and to gain insights into its internal structures. However, the study of snow transport is divided into two main categories: Lagrangian models, which focus on the motion of individual snow particles in the saltation layer near the snow surface, and turbulence diffusion models, which deal with the suspension layer. Notably, Nemoto and Nishimura (2001) developed a random flight model of blowing snow that incorporates turbulence, inertia of snow particles,



30 and particle size distribution. This model successfully captures the entire transition from the saltation layer to the suspension
layer during a blizzard. However, it is limited to steady-state conditions and does not address temporal and spatial variations.
To gain a more comprehensive understanding, it is crucial to consider organizational structures such as turbulence sweeps
and ejections when discussing the onset and development of snow transport. Unfortunately, the existing time-averaged
models based on local equilibrium theory and isotropic turbulence theory have limitations in grasping coherent structures
35 with regularity due to their restricted flow field representation.

Moreover, it has been observed that traffic accidents caused by reduced visibility on roads are strongly influenced by
temporal and spatial variations rather than the intensity of blowing snow itself. Consequently, the demand for models
capable of describing these temporal and spatial structures is widely recognized. Recently, efforts have been made to
develop models that combine Large-Eddy Simulation (LES) with Lagrangian snow transport models (e.g., Groot Zwaafink
40 et al., 2014 and Okaze et al., 2018). However, these models lack comprehensive measurements that adequately address the
high variability of these phenomena.

While a study by Aksamit and Pomeroy (2016, 2017) focused on temporal changes, it unfortunately lacked spatial
information. As a result, the reliability of these models remains unconfirmed, and our understanding of the high-frequency
fluctuations in the internal structures of blowing and drifting snow remains unsatisfactory. Against this backdrop, our study
45 aims to systematically measure blowing and drifting snow to investigate their spatiotemporal structures. To achieve this goal,
we have deployed fifteen Snow Particle Counters (SPCs) in designated test areas and are conducting measurements using an
equal number of ultrasonic anemometers, providing high temporal resolution data.

2 Field observation

The field observations were conducted during the winter of 2018 in Tobetsu, Hokkaido, Japan. Tobetsu is located close to
50 the coast of Ishikari bay and experiences strong monsoon winds from the west during the winter. The measurement
apparatus zone was situated in the windward area, where a flat snow field spreads over a distance of more than 200 meters
(Fig. 1).

Fifteen measurement towers were installed along a line perpendicular to the dominant wind direction, with each tower
spaced 1.5 meters apart. The towers were equipped with Snow Particle Counters (SPCs, SPC-7 and SPC 95, Niigata Denki
55 Co. Ltd) and Ultra Sonic Anemometers (USAs, Young 81000) to measure both the spatio-temporal structures of blowing
snow and the air flow (Fig. 1). The height of the SPCs was initially 39 cm, and the height of the USAs was 84 cm, but both
heights decreased with increasing snow accumulation.

The SPCs are typically used to obtain snow particle size distribution and mass flux at 1-second intervals. However, in this
study, the output signals from the SPC transducers were directly recorded with a high frequency of 100 kHz. This allowed
60 the researchers to calculate not only the mass flux but also the particle size and speed with fine time resolutions (Nishimura



et al., 2014) . The wind speeds measured with USAs were stored with a frequency of 1 kHz. To ensure accurate synchronization of time for both recordings, precise calibration and alignment were performed.

Other meteorological data, such as mean wind speeds and directions, and air temperature, were obtained from an Automatic Weather Station (AWS) located approximately 1 km away in the northwest (windward direction). Additionally, data on
65 precise precipitation were available from the Double Fence Intercomparison Reference (DFIR) set at the Ishikari Blowing-Snow Test Field by Civil Engineering Research Institute for Cold Region (CERI), located at a distance of nearly 4 km to the west. The DFIR data were primarily used to determine whether the observed phenomena were purely drifting or blowing snow or if they were accompanied by snowfall.

Overall, the field observations were conducted in a well-equipped measurement zone, allowing the researchers to collect
70 detailed data on blowing snow and atmospheric conditions, which are crucial for their study of spatio-temporal structures of blowing snow.

3. Results and analysis

In February 2018, meteorological conditions were recorded using AWS and DFIR, as depicted in Fig. 2. The red arrows indicate the duration of the intense observation period. Despite not having an exceptionally high wind speed at 2 meters
75 above the surface, the westerly wind was sufficient to initiate drifting/blowing snow. Throughout the period, the air temperature remained mostly below zero, causing the snow depth to increase from 80 to 110 cm in just one month. Consequently, the sensor height of the Snow Particle Counter (SPC) decreased from 39 to 1 cm due to the snow accumulation.

During the intense observation period, the Richardson number (Ri), calculated using vertical temperature and wind speed
80 profiles (Sutton, 1953), indicated neutral conditions ($Ri < |0.01|$).

Figure 3 illustrates the recordings of wind speed from the ultrasonic anemometer (USA) and snow mass flux, particle speed, and particle diameter obtained with the SPC at the spanwise direction $Y = 9$ m for 60 seconds. On February 16, the sensor heights for the USA and SPC were 91 cm and 23 cm, respectively, while on February 24, they were 76 cm and 8 cm. Although the sensor height of the USA is 70 cm higher than the SPC, the change in snow mass flux aligned well with the
85 wind speed on both days. Particularly, the response on February 24 was more pronounced, suggesting that the snow flux in the saltation layer is more sensitive to wind speed fluctuations than the one in the higher suspension layer. Figure 3 reveals that some particles move rapidly, even surpassing the wind speeds. These particles likely originate from higher positions, where they are accelerated by stronger winds. However, in general, particle speeds are lower than the wind speed, as reported in Nishimura et al. (2014), who found that mean particle speeds are consistently 1 m/s to 2 m/s less than wind
90 speeds at heights of 0.015 to 1 m. While particles smaller than 100 μm in diameter contributed more on February 16, they displayed a wide distribution within the range of 50 – 450 μm on February 24. Decreasing the height from the snow surface revealed larger particle numbers with a wide size distribution.



Figure 4 displays horizontal mass flux distributions, reflecting the spatio-temporal variability of blowing snow, measured with fifteen SPCs for 120 seconds on February 12, 16, and 24. The measured heights from the snow surface were 31 cm, 23
95 cm, and 8 cm, respectively. At the AWS point, wind direction was kept steadily as west and wind speeds at 2 m high on three days were nearly the same: from 4.5 to 5 m/s. Further, precipitations observed with DFIR were quite small and can be neglected. They show the maps of snow transport intensity, by lining up time series from the data of SPC transverse array in the spanwise Y direction and applying Taylor's frozen hypothesis (1938) to substitute time for the streamwise direction. Despite steady westward wind direction and similar wind speeds at 2 m height on the three days, the flux distributions were
100 neither uniform with time nor space and exhibited periodic changes. Figure 5, which shows pictures of the field's upstream at night on February 20, highlights the periodical snow waves approaching the sensors. These waves correspond to the periodical change in snow flux observed in Fig. 4.

On February 16 and 24, Figure 6 displays the blowing snow flux distributions for 10 seconds at heights of 23 cm, 8 cm, and 1 cm from the snow surface. Contrary to Fig. 4, as the height decreased from the surface, long and narrow structures
105 emerged prominently. These structures are similar to the phenomena known as "snow snakes," which meander laterally, merging and bifurcating as they move downwind, similar to observed phenomena in drifting sand movement. The height of the long structures along the snow surface varied, and taller parts occasionally protruded to higher positions, as seen in the cases of 23 cm and 8 cm in Fig. 6. Although the 1-meter spacing between SPCs did not provide sufficient resolution to be clear in the figure, it suggests that the structures at 1 cm above the surface had widths on the order of 2 meters and a lateral
110 spacing of about 1 meter. The propagation speed was roughly estimated to be 2 to 3 m/s based on particle speed data from analyzing the SPC data (Fig. 3b).

Figure 7 displays the power spectra of mass flux at $Y=10.5$ m for each measurement in Fig. 4, along with the ones for wind speeds. The dominant frequencies appeared to change from 0.1 Hz to 0.04 - 0.05 Hz as the height decreased from the snow surface. This suggests the presence of coherent structures, with sizes increasing from the suspension layer to the saltation
115 layer. The dominant frequencies and general trends of the power spectra for snow flux and wind speed appear very similar, implying that both vary in a correlated manner. Despite the sensor heights of SPCs being 31 cm lower than those of anemometers, these observations suggest that changes in snow flux reflect the structures of turbulence eddies near the snow surface.

To explore the correlation between snow transport and coherent structures in the boundary layer, Quadrant analysis was
120 applied. This classical analysis examines the fluctuating wind velocities of the streamwise and vertical components (u' and w') and their product, the Reynolds stress, to identify ejection Q2 ($u'<0, w'>0$), where lower-momentum air is expelled away from the bed, and sweep Q4 ($u'>0, w'<0$), where higher momentum air is pushed towards the bed, events contributing to turbulent energy production. Figure 8 shows the horizontal distributions of snow mass flux, wind speed, and ejection (Q4) and sweep (Q2) events on February 12 and 24, 2018. It is evident that large snow mass flux, corresponding to the ridge of
125 the snow wave (in Figure 5), occurs under conditions of high wind speeds and sweep events (Q4, $u'>0, w'<0$) on both days.



Figure 9 illustrates the correlation between the horizontal snow flux at 1 cm and the absolute value of the kinetic shear stress $u'w'$ in each quadrant on Feb. 24, 2018. The results indicate that snow fluxes were predominantly observed in quadrants Q1 ($u'>0, w'>0$) and Q4 ($u'>0, w'<0$), while being far less prominent in quadrants Q2 and Q3. Table 1 displays the contributions of each quadrant, acquired on February 12, 16, and 24, at corresponding heights from the snow surface: 31 cm, 16 cm, 8 cm, and 1 cm. Ejection-like events (Q2: $u'<0; w'>0$) and sweep-like events (Q4: $u'>0; w'<0$) contributed 12% to 22% and 33% to 48%, respectively. Q4 exhibited the largest contribution, while Q1 consistently followed in all events, regardless of the height from the surface. Moreover, the combined contributions of Q1 and Q4 account for over 64%, while Q2 and Q3 contribute less than 36%. The contributions from quadrants Q2 and Q3 ($u'<0; w'<0$) were notably smaller compared to the significant impact of Q1 and Q4. In contrast, Figure 10 illustrates the distributions of the snow mass flux at 1 cm, as well as the wind speed, ejection, and sweep structures at 40 cm for a 10-second on February 24. The data indicates that the foremost region of the snow snake primarily aligns with the ejection phenomenon, trailed closely by the sweep motion. For a more detailed examination of the structures preceding and during the onset of transport escalation, specific ten-second sub-periods (marked with arrows in Fig. 8 and whole durations in Fig.10) have been extracted and presented in Figure 11. Figures 11 (a) to (e) present the wind speeds and mass fluxes at $Y=4.5$ m, 10.5 m, and 15.0 m from 25 to 35 s and at $Y=10.5$ m and 15.0 m from 60 to 70 s in Fig. 8. Furthermore, using the approach introduced by Aksamit and Pomeroy (2017), parametric curves of $(u'(t), w'(t))$ were displayed, representing the duration of the time indicated by arrows in each figure: from 30 to 35 s for the former and from 67 to 70 s for the latter. These curves were plotted every one second with different colours.

For example, in Figure 11 (a), no snow transport occurred between 30 to 31s at $Y=4.5$ m, followed by an abrupt increase in snow flux. Afterward, the mass flux diminished to nearly zero from 31.5s to 32.5s, and then increased again from 33 to 34s. The parametric curve of $(u'(t), w'(t))$, encompassing the entire first peak of the horizontal mass flux (pre-increase, increase, and decrease) between 30 to 33 seconds, was situated within quadrant Q2 (ejection region). However, the second increase occurred in quadrants Q1 and Q4, characterized by stronger horizontal wind speeds. Similarly, at $Y=10.5$ m in Fig. 11 (b), from 32 to 34 s, the parametric curve mainly remained in Q2, covering the duration before the increase and the flowing period leading to the maximum, and then moved to Q1. In Fig. 11 (c), which shows the case at $Y = 15.0$ m, the snow flux started to increase at 33 s. The parametric curve was mostly in Q4 one second before. However, at the onset of the increase at 33 s, it shifted to Q2 and later moved to Q1. Figure 11 (d) illustrates the case at $Y=10.5$ m from 60s to 65s, where the snow flux started to increase at 68 s and reached its peak at 69.1 s. The parametric curve from 67 to 70 s indicated that both periods, one second before the increase in snow transport and the path to the maximum, were in Q2, and it subsequently moved to Q1 and Q4 where the horizontal wind speed was greater. The snow flux change at $Y=15.0$ m shown in Fig. 11e was almost similar to that at $Y=10.5$ m. Although the staying period of the parametric curve in Q2 was rather short compared to other cases, it was on Q2 during both the period just prior to the increase in mass flux and the front part, and then it shifted to Q1 and Q4. Overall, the parametric curve patterns indicated that the ejection part Q2 exists both prior to the snow waves and at the nose of the snow snake, while Q1 and Q4, where horizontal wind speed is higher, follow.



160 In Fig. 12, structures around the snow snake are displayed, showing wind speed and snow flux for ten seconds at $Y=15.0$ m
and the parametric curve from one to 6 s. The front of the snow snake arrived at the sensor at around 2.5 s, and the snow flux
increased rapidly. During 1 to 2 s, the parametric curve remained in Q1, but it shifted to Q2 just in front of the snake head,
then moved to Q1 and Q4. It's worth noting that the curve briefly returned to Q2 before the second mass flux peak. During
the flowing period, the curve predominantly stayed in Q1 and Q4, where u' is positive. In general, the parametric curve
165 follows the ejection part Q2 in front of the snake head and then shifts to Q1 and Q4, similar to the snow wave behaviour in
Figs. 11 (a) to (e).

4 Results and analysis

We conducted systematic measurements of blowing snow, which allowed us to reveal the spatiotemporal structures of the
170 phenomenon. In comparison, research on sand transport, particularly aeolian streamers, has been explored in studies such as
Bauer et al. (1998) and Sterk et al. (1998). Bauer et al. (1998) used a hot-wire anemometer and load-cell sand traps,
identifying three typical transport patterns: streamer families, nested streamers, and clouds with embedded streamers.
However, these latter two patterns occurred only at high shear velocities. Comparing their classification with our study's
findings in Figs. 4 and 5, the structures observed on February 16 and 24 likely correspond to streamer families and nested
175 streamers. Yet, 'clouds with embedded streamer' was not found in the snow transport, likely because the wind speeds were
relatively low and insufficient to transport large amounts of snow particles. It is worth noting that the periodical changes in
snow flux shown in Fig. 4 were not mentioned in Bauer et al. (1998), possibly because their focus was on phenomena
occurring within a short period of five seconds, while the snow waves recognized in Fig. 4, with frequencies less than 0.1 Hz,
were observed over 40 seconds.

180 In their study, Bauer et al. (1998) also conducted quadrant analysis and found that ejection-like events (Q2: $u' < 0$; $w' > 0$)
and sweep-like events (Q4: $u' > 0$; $w' < 0$) contributed 39.5% and 50.6%, respectively, to the total kinematic Reynolds-shear
stress, with the combined contribution reaching 90.1%. This heavily skewed the quadrant ellipses toward the Q2 and Q4
quadrants, indicating that horizontal velocity fluctuations (u') were more important for snow transport than vertical velocity
fluctuations (w'). Similar results were reported by Sterk et al. (1998), who used a Gill-type anemometer and acoustic
185 sediment sensing instruments. They also found that contributions from Q1 ($u' > 0$; $w' > 0$) and Q3 ($u' < 0$; $w' < 0$) quadrants
were significantly smaller compared to Q2 and Q4 contributions. Our studies align with these findings, as shown in Table 1,
where contributions from Q1 and Q4 quadrants were significantly larger than those from Q2 and Q3, supporting the idea that
horizontal velocity fluctuations (u') play a crucial role in aeolian sediment transport compared to vertical fluctuations (w') or
kinematic shear stress ($u'w'$).

190 Baas and Sherman (2005) applied the Variable Internal Time Averaging method (VITA) to wind speed data, which identifies
significant turbulent events using local variance within a moving time window (Blackwelder and Kaplan, 1976). They found
that VITA events were generally poorly correlated with transport events, and sweep-like motions with strongly positive u'



signals dominated over ejection-like motions. Then, they interpreted the streamer patterns have a probable origin in large 'eddy surface layer', where turbulent eddies from higher regions of the atmospheric boundary layer travel downward, elongate and stretch out in the shear layer, and scrape across the surface. Later, Hunt and Morrison (2000) proposed a top-down model of boundary layer turbulence for very high Reynolds number flows. Aksamit and Pomeroy (2017) also applied quadrant analysis and VITA techniques to their snow transport measurements, revealing that sweeps were the dominant motion for initiating blowing snow and increasing concentration and particle number flux near the surface. Active ejections occurred during active blowing snow and after sweeps.

Our measurements also represents that the snow fluxes were observed largely in Q1 ($u'>0, w'>0$) and Q4 ($u'>0, w'<0$) quadrants. However, we should note that the detailed analysis with the parametric curve revealed that the ejection part Q2 exists both prior to the snow waves (in Figs. 10a to e) and in front of the snake head (in Fig. 14), and then shifts to the Q1 and Q4, where horizontal wind speed becomes larger. Thus, in addition to the top-down mechanism proposed by Baas and Sherman (2005), bottom-up mechanisms of burst sweep events cannot be ruled out at this stage. Detailed measurements, such as setting the SPCs and USAs at the same height from the surface the height, and Spatiotemporal the introduction of most up-to-date turbulence analysis technique will be helpful to deepen our understanding and reach the conclusion. Further, not only the horizontal but also the vertical spatiotemporal structures of blowing snow need to be investigated.

As stated in the introduction, time-averaged blowing snow models have limitations, necessitating the incorporation of relationships with organizational structures such as turbulence sweeps and ejections to discuss the onset and development of snowstorms more accurately. Models that can describe temporal and spatial structures are crucial. To address this, we have developed the Large-Eddy Simulation coupled with Lagrangian Snow Transport model LLAST (Okaze et al., 2020). This model combines large-eddy simulation for turbulent flow and particle translational simulations based on Newton's equations of motion. The field observations and analysis presented in this study will significantly contribute to the improvement and validation of the model.

215

Data availability

All raw data can be provided by the corresponding authors upon request.

Author contributions.

KN and MN planned the project; KN and MN, YI, SO, KS, and HN took part in the observations; KN and MN analyzed the data; KN wrote the manuscript.

Competing interests. The contact author has declared that neither of authors has any competing interests.

225

Acknowledgements.



The authors extend their heartfelt gratitude to the Tobetsu local government for their generous permission to utilize the managed park area as the observation field. Additionally, our sincere appreciation goes out to all our colleagues for their invaluable support in conducting the field measurements. This collaborative effort played a pivotal role in successfully completing this research endeavor.

References

- Aksamit, N. O. and Pomeroy, J. W.: Near-surface snow particle dynamics from particle tracking velocimetry and turbulence measurements during alpine blowing snow storms, *The Cryosphere*, 10, 3043–3062, <https://doi.org/10.5194/tc-10-3043-2016>, 2016.
- 235 Aksamit, N. O. and Pomeroy, J. W.: The Effect of Coherent Structures in the Atmospheric Surface Layer on Blowing-Snow Transport, *Boundary Meteorol.*, 167, 211–233, <https://doi.org/10.1007/s10546-017-0318-2>, 2017.
- Aksamit, N. O. and Pomeroy, J. W.: Scale Interactions in Turbulence for Mountain Blowing Snow, *J. Hydrometeorol.*, 19, 305–320, <https://doi.org/10.1175/JHM-D-17-0179.1>, 2018.
- Baas, A. C. W. and Sherman, D. J.: Formation and behavior of aeolian streamers, *Journal of Geophysical Research*, 110, F03011, [doi:10.1029/2004JF000270](https://doi.org/10.1029/2004JF000270), 2005.
- 240 Baas, A. C. W. and Sherman, D. J.: Spatiotemporal variability of aeolian sand transport in a coastal dune environment, *Journal of Coastal Research*, 22, 1198–1205, 2006.
- Bauer, B., Yi, J., Namikas, S., and Sherman, D.: Event detection and conditional averaging in unsteady aeolian systems, *J. Arid Environ.*, 39, 345–375, 1998.
- 245 Bauer, B., Yi, J., Walker I. J., Baas, A. C. W. et al.: Critical reflections on the coherent flow structures paradigm in aeolian geomorphology, In: Venditti, J. G., Best, J. L., Church, M., and Hardy, R. J. (eds), *Coherent flow structures at earth's surface*, Wiley Blackwell, West Sussex, pp 111-134, 2013.
- Blackwelder, R., and Kaplan, R.: On the wall structure of the turbulent boundary layer, *J. Fluid Mech.*, 79, 89-112. 1976.
- Elliot, W. P.: The growth of the atmospheric internal boundary layer, *Eos Trans. AGU*, 39 1048-1054, 1958.
- 250 Groot Zwaafink, C. D., Diebold, M., Horender, S., Overney, J., Lieberherr, G., M. B. Parlange, M. B., and Lehning, M.: Modelling Small-Scale Drifting Snow with a Lagrangian Stochastic Model Based on Large-Eddy Simulations, *Boundary-Layer Meteorology* volume 153, 117–139. <https://doi.org/10.1007/s10546-014-9934-2>, 2014.
- Hunt, J. C. R. and Morrison J. F.: Eddy structure in turbulent boundary layers. *Eur. J. Mech. B-Fluids* 19, 673-694. [https://doi.org/10.1016/S0997-7546\(00\)00129-1](https://doi.org/10.1016/S0997-7546(00)00129-1), 2000.
- 255 Leenders, J. K., van Boxel, J. H., and Sterk, G.: Wind forces and related saltation transport. *Geomorphology* 71,357-372, 2005.
- Nemoto, M. and Nishimura, K.: Numerical simulation of drifting snow in turbulent boundary layer, *Journal of Geophysical Research*, 109, 18206-18219, 2004.



260 Nishimura, K., Yokoyama, C., Ito, Y., Nemoto, M., Naaïm-Bouvet, F., Bellot, H., and Fujita, K., Snow particle speeds in drifting snow, *Journal of Geophysical Research, Atmos.*, Vol. 119, doi:10.1002/2014JD021686, 2014.

Okaze, T., Niiya, H., and Nishimura, K.: Development of a large-eddy simulation coupled with Lagrangian snow transport model, *Journal of Wind Engineering and Industrial Aerodynamics*, Vol. 183, 35-43, <https://doi.org/10.1016/j.jweia.2018.09.027>, 2018.

Sutton, O. G.: *Micrometeorology*, 333 pp., McGraw-Hill, New York, 1953.

265 Taylor, G. I.: The spectrum of turbulence, *Proc. R. Soc. London, Ser. A*, 164, 476-490, 1938.

Shonfeldt, H. J., and von Lowis, S.: Turbulence-driven saltation in the atmospheric boundary layer. *Meteorologische Zeitschrift* 12, 257-268, 2003.

Sterk, G., Jacobs, A. F. G., and van Boxel, J. H.: The effect of turbulent flow structures on saltation sand transport in the atmospheric boundary layer, *Earth Surf. Processes Landforms*, 23, 877-887, 1998.

270

275 **Table 1. Contributions of each quadrant on February 12, 16, and 24, at corresponding heights of mass flux from the snow surface: 31 cm, 16 cm, 8 cm, and 1 cm.**

Figure 1. Observation field: Tobetsu, Hokkaido, Japan (left). Measurement apparatus: fifteen Snow Particle Counters (SPCs) and Ultra Sonic Anemometers (USAs) set on towers 1.5 m apart (right).

280

Figure 2. Meteorological conditions at the observation site in February 2018. Red arrows indicate the duration of the intense observation period.

285 **Figure 3. Time series of wind speed, snow mass flux, particle speed, and particle diameter at the spanwise direction $Y = 9$ m. a: on February 16, the sensor heights for the USA and SPC were 91 cm and 23 cm, b: on February 24, 76 cm and 8 cm.**

Figure 4. Horizontal mass flux distributions for 120 sec., reflecting the spatio-temporal variability of blowing snow, on February 12, 16, and 24. The measured heights from the snow surface were 31 cm, 23 cm, and 8 cm, respectively.

290

Figure 5. ‘Snow waves’ appeared on the field's upstream at night on February 20 (above) and ‘snow snake’ (below).



Figure 6. Horizontal mass flux distributions for 10 seconds at heights of 23 cm, 8 cm, and 1 cm from the snow surface.

295 **Figure 7. Power spectra of mass flux and wind speeds at $Y=10.5$ m on February 12, 16, and 24**

Figure 8. Horizontal distributions of snow mass flux, wind speed, and ejection (Q4: red) and sweep (Q2: blue) events on February 12 and 24, 2018.

300 **Figure 9. Correlation between the horizontal snow flux at 1 cm and the absolute value of the kinetic shear stress $u'w'$ in each quadrant on Feb. 24, 2018.**

Figure 10. Distributions of the snow mass flux at 1 cm, as well as the wind speed, ejection, and sweep structures at 40 cm for a 10-second on February 24.

305

Figure 11. (a) to (e) present the wind speeds and mass fluxes at $Y=4.5$ m, 10.5 m, and 15.0 m from 25 to 35 s and at $Y=10.5$ m and 15.0 m from 60 to 70 s in Fig. 8. Furthermore, parametric curves of $(u'(t), w'(t))$ were plotted every one second with different colours for the period indicated by arrows in each figure: from 30 to 35 s for the former and from 67 to 70 s for the latter.

310

Figure 12. Structures around the snow snake: wind speed, snow flux for ten seconds at $Y=15.0$ m, and the parametric curve from one to 5 s in Fig. 10.

Table 1. Contributions of each quadrant on February 12, 16, and 24, at corresponding heights of mass flux from the snow surface: 31 cm, 16 cm, 8 cm, and 1 cm.

Date	Feb. 12	Feb. 16	Feb. 24	Feb. 24
Sensor height	16 cm	23 cm	8 cm	1 cm
Q1	0.30	0.30	0.33	0.28
Q2	0.22	0.23	0.12	0.21
Q3	0.12	0.14	0.07	0.15
Q4	0.36	0.33	0.48	0.36
Q1+Q4	0.65	0.64	0.81	0.64
Q2+Q3	0.35	0.36	0.19	0.36





Figure 1. Observation field: Tobetsu, Hokkaido, Japan. the measurement zone is indicated with an orange frame (left). Measurement apparatus: fifteen Snow Particle Counters (SPCs) and Ultra Sonic Anemometers (USAs) set on towers 1.5 m apart (right).

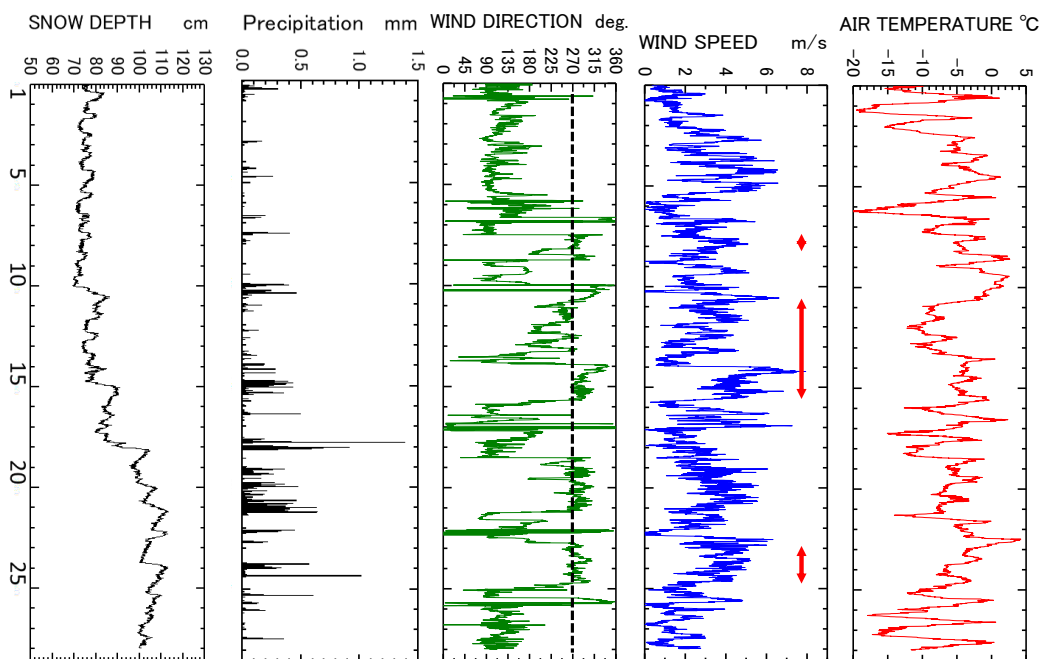


Figure 2. Meteorological conditions at the observation site in February 2018. Red arrows indicate the duration of the intense observation period.

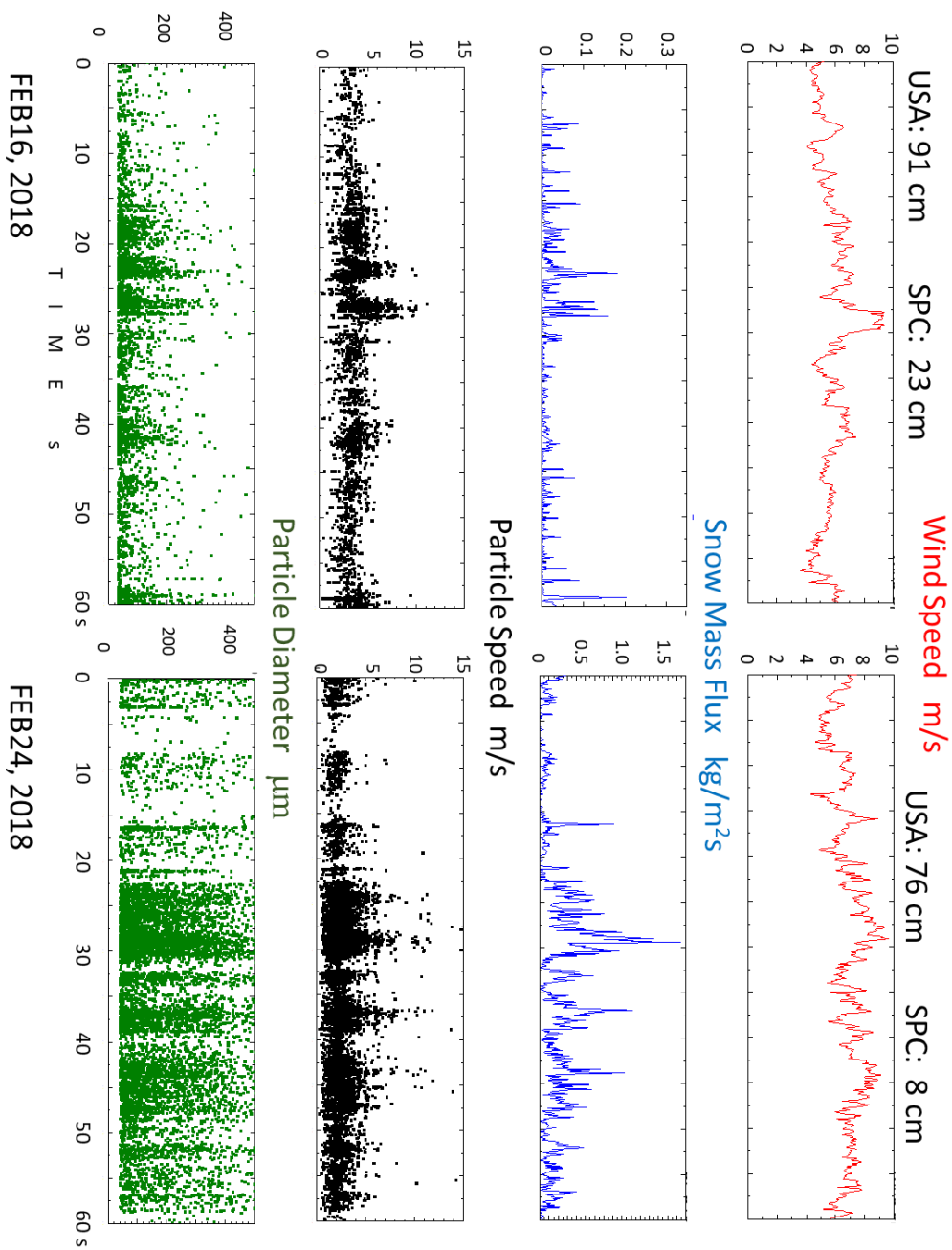


Figure 3. Time series of wind speed, snow mass flux, particle speed, and particle diameter at the spanwise direction $Y = 9$ m. a: on February 16, the sensor heights for the USA and SPC were 91 cm and 23 cm, b: on February 24, 76 cm and 8 cm.

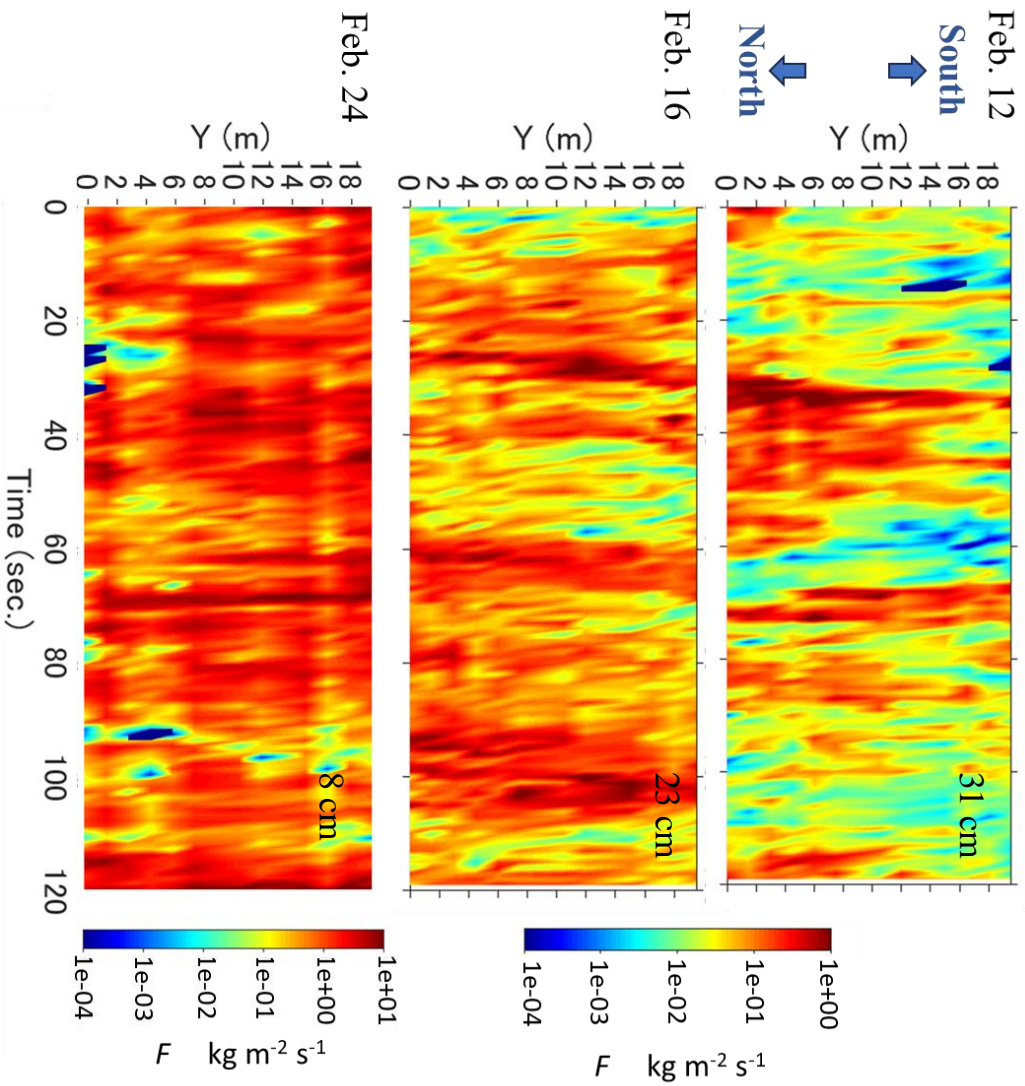
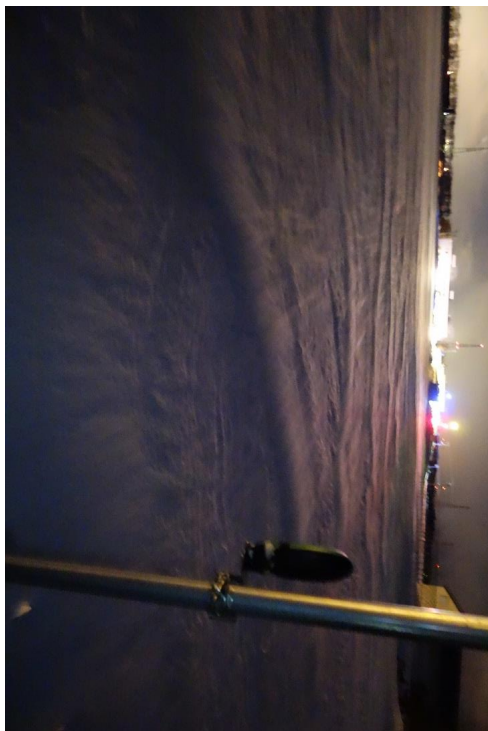


Figure 4. Horizontal mass flux distributions for 120 sec., reflecting the spatio-temporal variability of blowing snow, on February 12, 16, and 24. The measured heights from the snow surface were 31 cm, 23 cm, and 8 cm, respectively.



Figure 5. ‘Snow waves’ appeared on the field’s upstream at night on February 20 (above) and ‘snow snake’ (below).



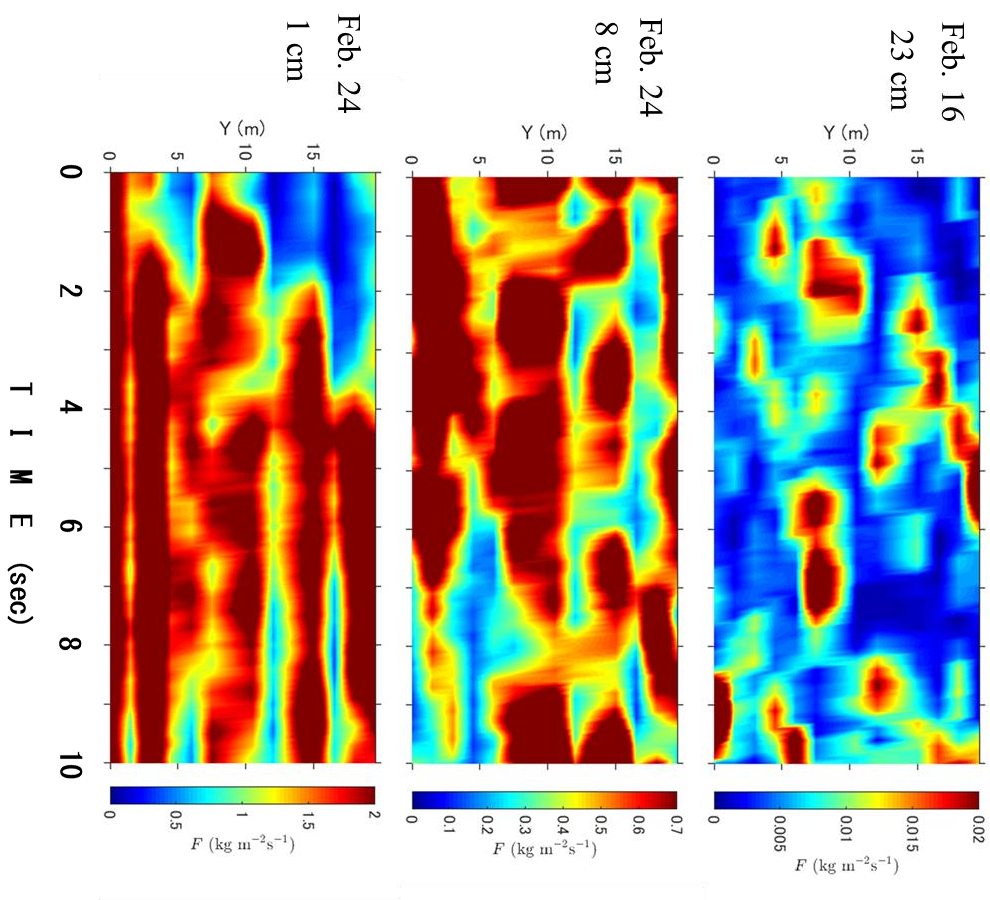


Figure 6. Horizontal mass flux distributions for 10 seconds at heights of 23 cm, 8 cm, and 1 cm from the snow surface.

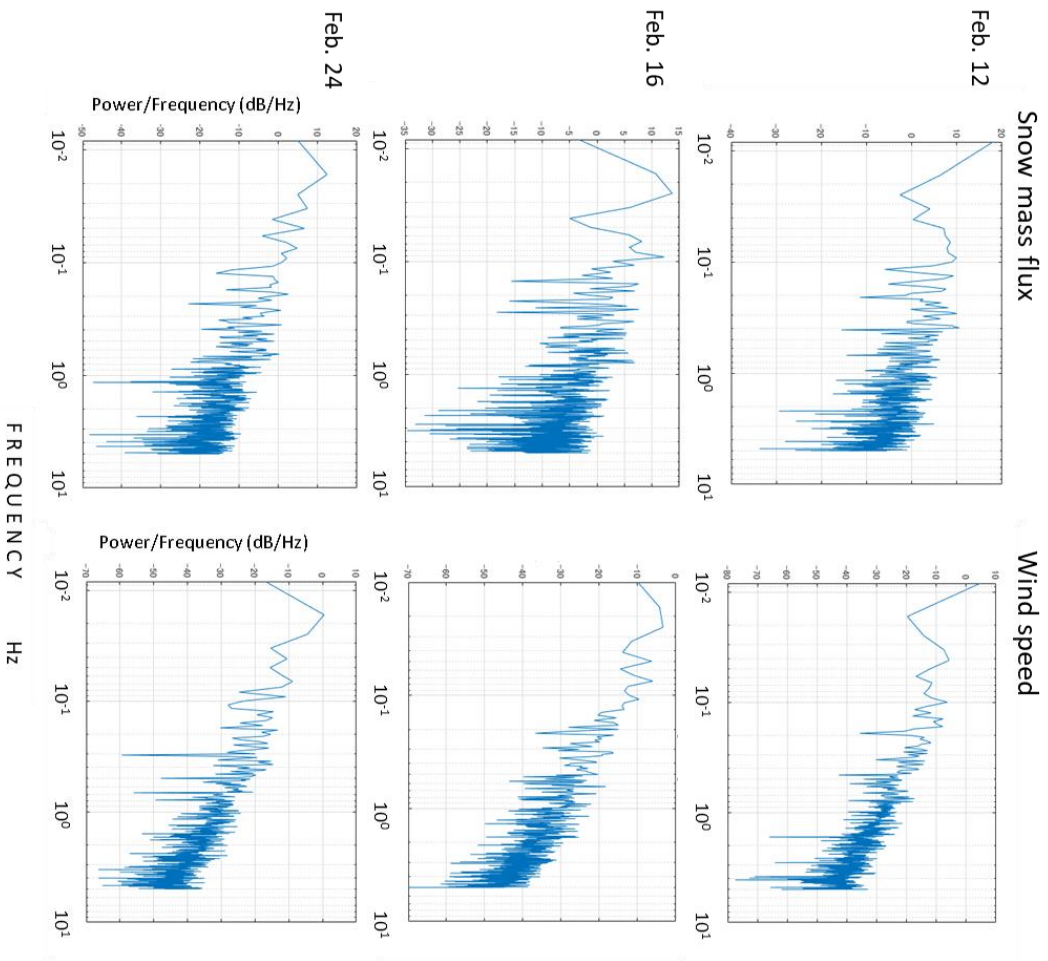


Figure 7. Power spectra of mass flux and wind speeds at Y=10.5 m on February 12, 16, and 24

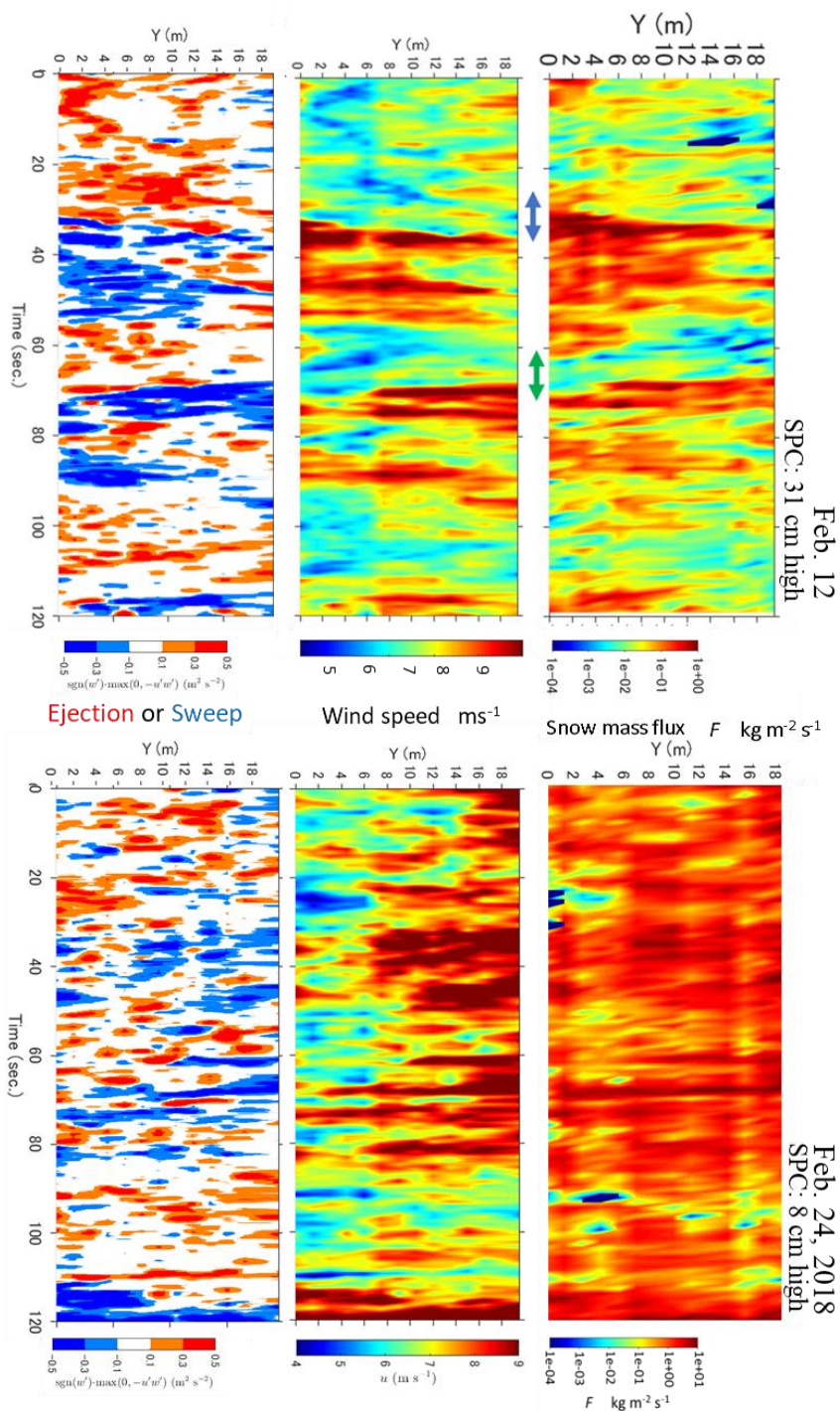


Figure 8. Horizontal distributions of snow mass flux, wind speed, and ejection (Q4: red) and sweep (Q2: blue) events on February 12 and 24, 2018.

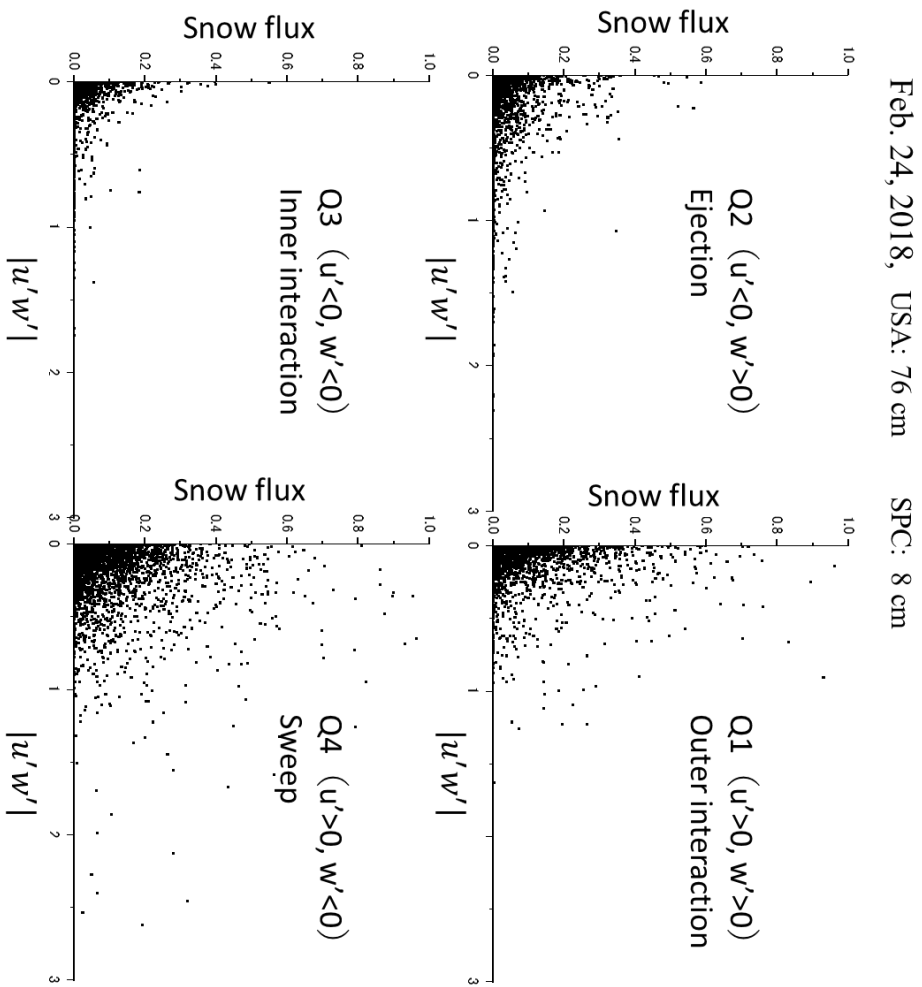


Figure 9. Correlation between the horizontal snow flux at 1 cm and the absolute value of the kinetic shear stress $u'w'$ in each quadrant on Feb. 24, 2018.

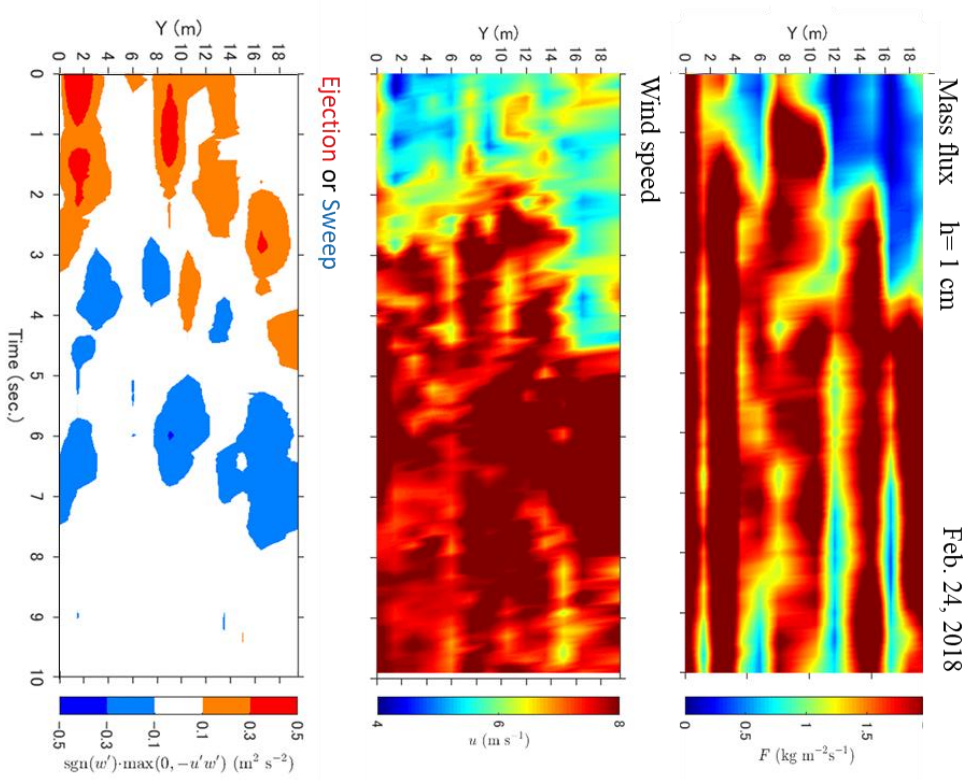
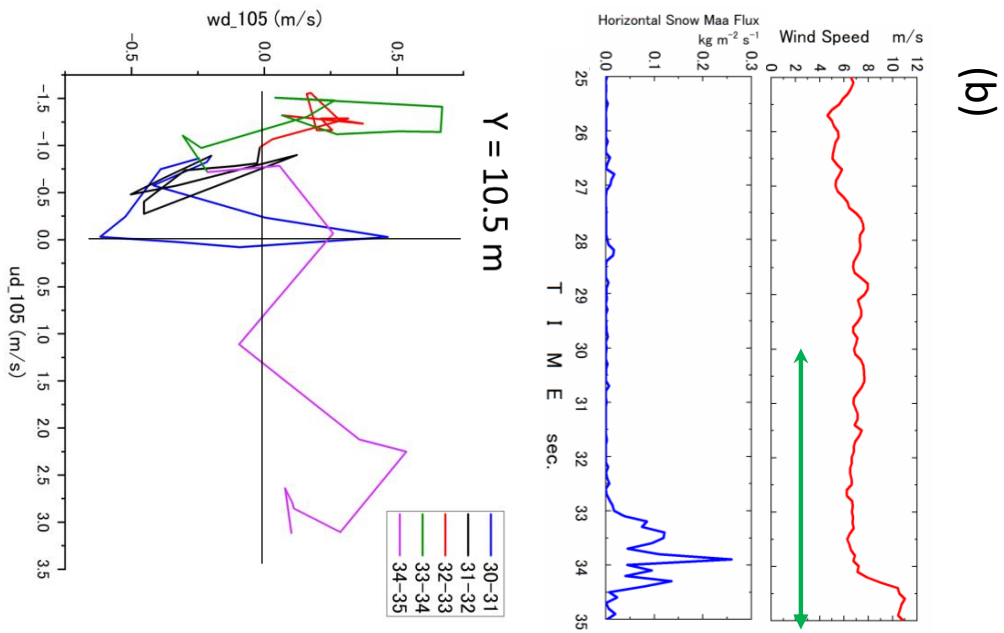
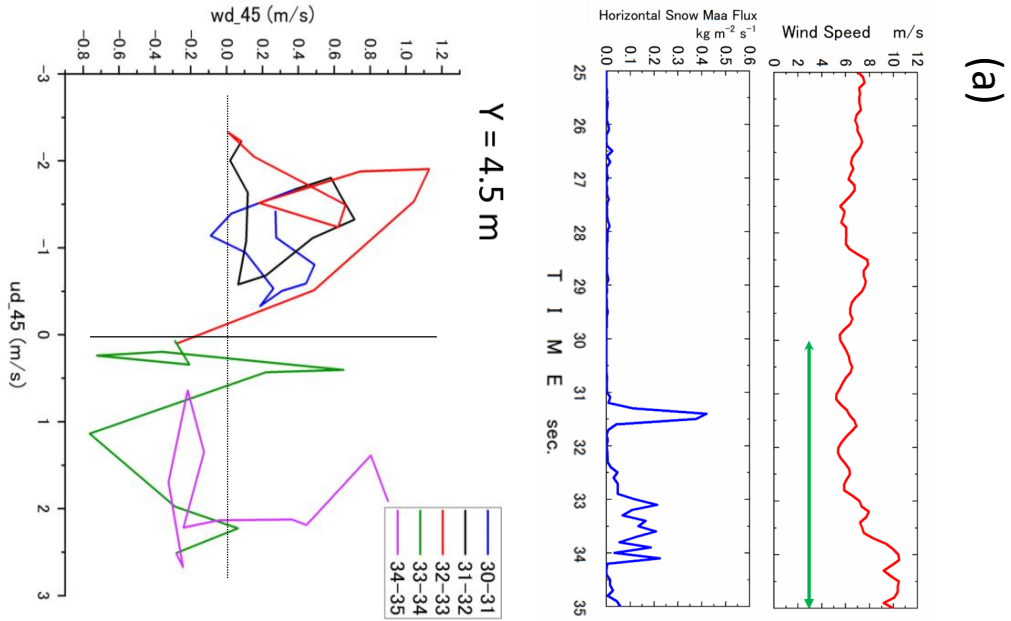
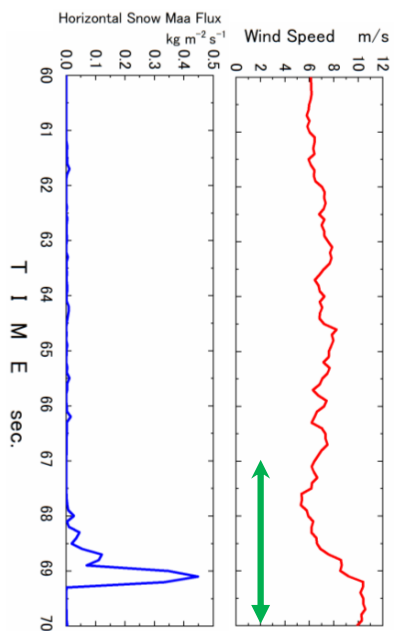
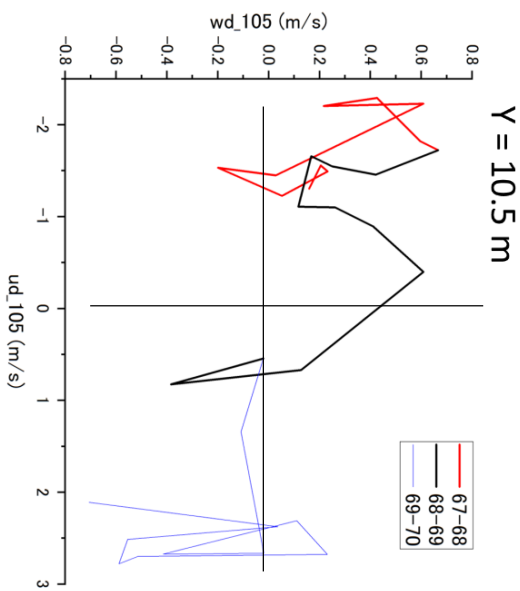
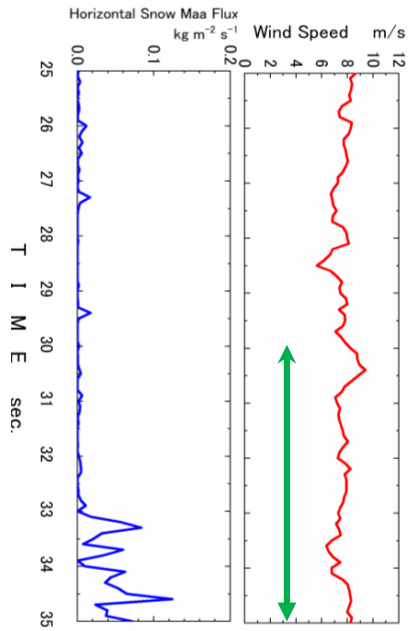
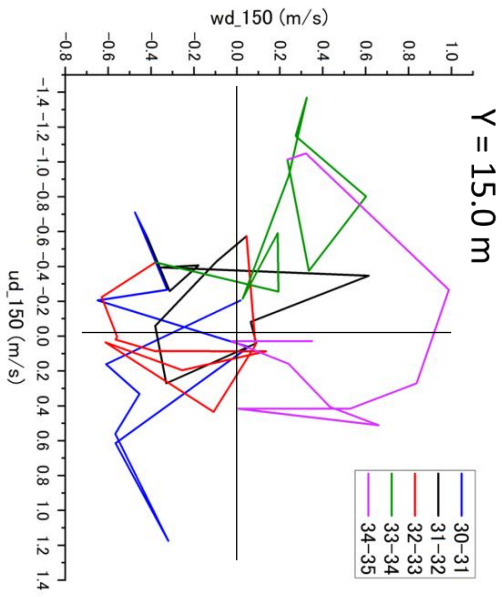


Figure 10. Distributions of the snow mass flux at 1 cm, as well as the wind speed, ejection, and sweep structures at 40 cm for a 10 second on February 24.





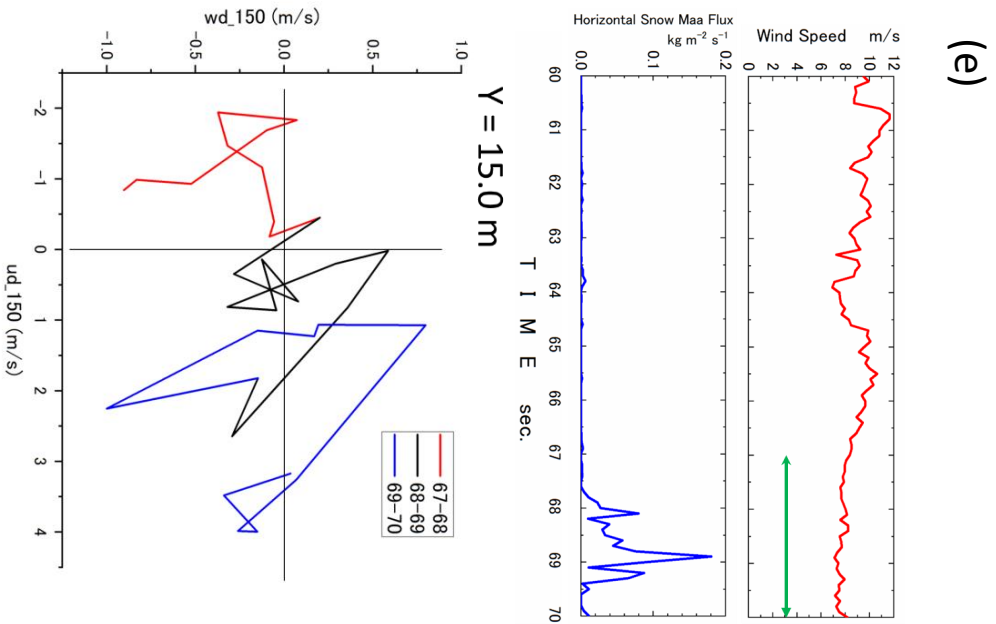


Figure 11. (a) to (e) present the wind speeds and mass fluxes at $Y=4.5$ m, 10.5 m, and 15.0 m from 25 to 35 s and at $Y=10.5$ m and 15.0 m from 60 to 70 s in Fig. 8. Furthermore, parametric curves of $(u^i(t), w^i(t))$ were plotted every one second with different colours for the period indicated by arrows in each figure: from 30 to 35 s for the former and from 67 to 70 s for the latter.

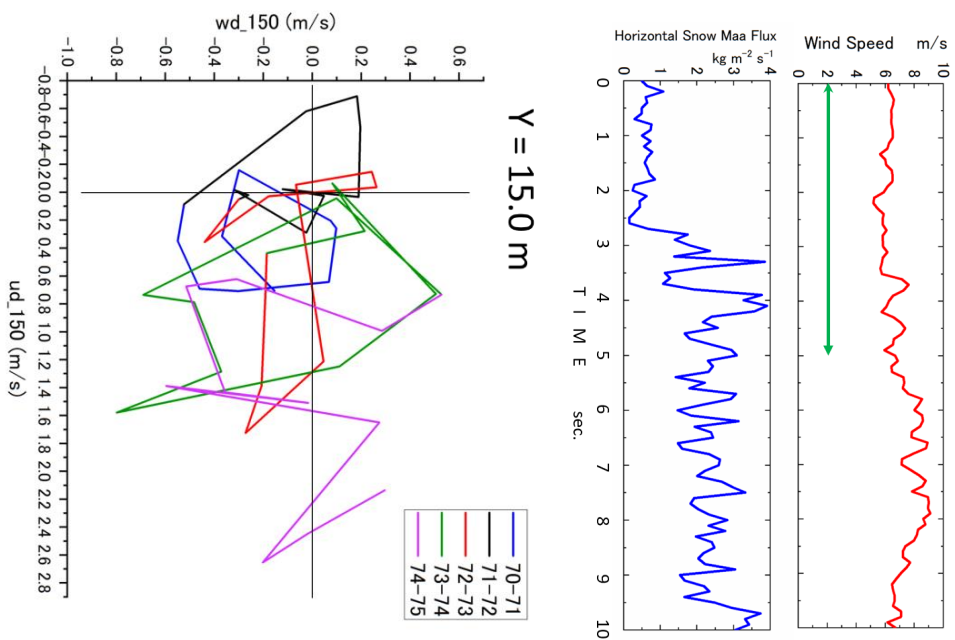


Figure 12. Structures around the snow snake: wind speed, snow flux for ten seconds at $Y=15.0$ m, and the parametric curve from one to 5 s.